Chapter 5: Dielectric and mechanical properties

5.1 Introduction

In the previous chapters, it has been established that with a suitable choice of masterbatch composition, host composition, and thermal history, a wide range of superlamellar morphologies can be generated. It may therefore be possible to exploit this fact in the design of engineering materials, although to do so would be beyond the scope of this thesis. The next two chapters are concerned instead with evaluating the suitability of these materials for electrical engineering applications as they stand. In order to impart the simplest reproducible thermal history to the materials, all samples in this chapter were quenched following pressing at 180 °C. Firstly, low voltage dielectric and low strain mechanical experiments are discussed; these probe the material behaviour in equilibrium. Such properties can be considered as intrinsic to the materials above a certain critical length (charge transport) or volume (molecular relaxation). The response of the materials to extreme mechanical and electrical stresses will then be discussed.

The response of a polymer to an alternating electrical field is determined by mechanisms operating on time scales ranging from electronic polarisation ($>10^{15}$ Hz) to the interfacial polarisation of mobile ions [5.1]. Electrical engineers are primarily concerned with the response around power frequencies, where molecular motion occurs. Consequently, permittivity and loss characteristics can be strongly affected by morphological features. Another consequence is the likely connection between mechanical and electrical responses in this frequency range. However, significant differences occur because of the manner in which the system couples with the field: electrical dipoles couple directly to an applied electrical field, whereas mechanical stress is mediated by the system itself. Consequently, creep effects become increasingly pronounced with reducing frequency in mechanical systems.

If a group of non-interacting molecular subsystems exists with a single characteristic time τ and an exponential approach to equilibrium, its complex susceptibility will obey the following form [5.2]:

$$\chi^*(w) = \frac{\Delta\varepsilon}{1+\omega^2\tau^2} - j\left[\frac{\Delta\varepsilon\omega\tau}{1+w^2\tau^2} + \frac{\sigma}{\varepsilon_0\omega}\right] = \varepsilon_r - 1 \qquad (5.1)$$

where $\Delta\varepsilon$ is the low frequency susceptibility, ε_r the relative permittivity, ω the field frequency and σ a field-independent conductivity corresponding to charge carrier motion. This latter term will appear as a slope of -1 on a double-log plot of imaginary permittivity against frequency. The ratio energy loss per cycle: energy stored per cycle can be expressed:

$$Tan(\partial) = \frac{\varepsilon_r''}{\varepsilon_r'} \qquad (5.2)$$

where δ is the angle by which the current leads the applied voltage. Provided the high frequency permittivity ε_{HF} is sufficiently large, the loss peak can be considered as having the same frequency as the imaginary permittivity peak. This is demonstrated in Figure 5.1 below.

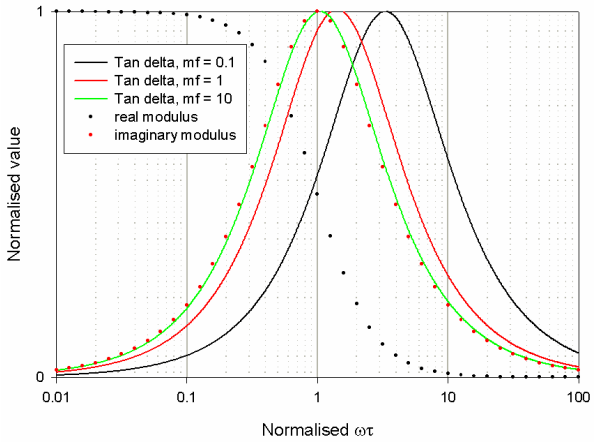

Figure 5.1: Comparison of real, imaginary and tan-delta Debye responses for various values of high frequency permittivity ε_{HF}. (For example mf=10 = "multiplication factor = 10" is the case where $\varepsilon_{HF} = 10\ \Delta\varepsilon_{Debye}$. Provided this is the case, the difference in frequency location between imaginary permittivity and tan-delta is negligible.)

In our systems, this means that the data can be plotted in terms of tan-delta as a more useful engineering parameter than imaginary permittivity.

In equation (5.1) the permittivity and conductivity terms can be considered independently. This will not be the case if charge storage at internal boundaries results in a modification of the local field. If a monodisperse second phase is introduced in to a matrix, a Debye-shaped relaxation results, provided that the conductivity of the included phase is significantly greater than the matrix. This is the so-called Maxwell-Wagner-Sillars (MWS) relaxation [5.3]. If the complex permittivity is plotted on an Argand diagram known as a Cole-Cole plot [5.4], a Debye-type relaxation will yield a semicircle in the first quadrant with its circular centre located on the real axis. Conversely, a frequency-independent conduction process will introduce a vertical asymptote into the plot.

In general, the resolution of distinct single relaxation time processes is impossible, and the concept of distributions of linearly superposed relaxation times is commonly invoked [5.5]. The technique is purely empirical, and in the early 1980s Jonscher [5.6] and Dissado / Hill [5.7] began to argue powerfully against it. By collating a large amount of data from various disciplines, they noticed that there appeared to be a general law underlying the data which can be expressed as follows:

$$\chi''(w) = kw^{m} \qquad \omega << \omega_p$$

$$\chi''(w) = kw^{n-1} \qquad \omega >> \omega_p \qquad (5.3)$$

where k, m and n are constants and $0 < m < 1$, $0 < n < 1$. These relationships, which predict a response in fractal time, are a consequence of many-body interactions. In other words, for every dipole transition, the entire energy map of the system is altered. Specifically, this can be a result of fast intra-cluster and slow inter-cluster interactions which give rise to m and n respectively. However, Weron [5.8] has demonstrated that equation (5.3) can result from purely mathematical considerations of the stochastic properties of relaxation, regardless of the underlying physical processes.

Polyethylene demonstrates three principal relaxations. In order of increasing temperature (or frequency) these are designated the γ (-130 °C), *ß* (-20 °C) and *α* (~80 °C) relaxations respectively. They are reviewed in detail by Boyd [5.9] and Gradin *et al.* [5.10]. Systematic variations in sample composition have shown that while the *γ* and *ß* relaxations are concerned primarily with the amorphous regions, the *α* relaxation is a crystalline phenomenon. It comprises a chain rotation of 180 ° followed by a translation of half a unit cell, requiring 12 CH_2 units to preserve crystallographic register. Dielectrically, this can be achieved by the rotation of C=0 dipoles; on the other hand, the mechanical relaxation is driven by the translation motion of tie chains. Hence the mechanical process occurs, at 50 °C for example, around three orders of magnitude more slowly than the dielectric process. Note that if the polyethylene is not lightly oxidised, or otherwise rendered polar, it will not demonstrate any electrical relaxations.

5.2 Dielectric spectroscopy

Dielectric spectroscopy was performed using a Schlumberger 1290 frequency response analyser with a Solartron 1260A low-frequency bridge to extend the frequency range to low values. The function of the latter is to improve accuracy by comparing each signal with that obtained from a capacitor automatically selected from an internal bank. Samples were melt-pressed to a thickness of 410 ± 5 μm and quenched. An LDPE reference sample was also prepared. They were placed in a vacuum oven overnight at 40 °C in order to remove any water from the quench process. The samples were then left to equilibrate to atmospheric conditions for ~3 h. A paper mask was used during the sputter coating process in order to preserve an insulating 1 mm annulus around the edge of the 30 mm diameter samples. The sputter coating served the purpose of maintaining uniformity in the electrical contact geometrically across the surface and reproducibility of the local electrical characteristics of the electrode-sample junction.

Due to the low loss nature of polyethylene, it was found that normalisation served only to increase the amount of noise in the imaginary

permittivity. Ten cycle integrations per point proved sufficient for de-noising. Initial experiments were performed whereby the driving voltage was increased logarithmically from 0.01 to 3 V rms to check for linearity. It was found that the best compromise between noise and signal clipping vulnerability was found at 1 V rms.

Figure 5.2 shows the effect of masterbatch composition and loading level on capacitance tan-delta. There are several important features here:

● The degradation processes as picked up by Raman spectroscopy (chapter 2) have not significantly increased the dielectric loss.

● A small conduction current is present in the unfilled materials below 1 Hz, appearing as a straight line at low frequencies; this is the rationale for using a log scale for tan-delta in Figure 5.2. The corresponding conductivity is ~10^{-15} S cm^{-1} which is a typical value for the bulk conductivity of PE [5.11]. This effect is too small to be seen in the filled materials, confirming that a 3-terminal cell was not required to divert surface conduction currents to ground. It is remarkable that the measured conductivity was not higher than this due to surface conduction over the inside walls of the PTFE jacket.

● The dielectric loss is strongly influenced by masterbatch loading level, and less strongly by masterbatch chemistry. At power frequencies, for example, tan-delta is ~2 orders of magnitude higher in NB20 and NC20 than in the unfilled materials.

Figure 5.3 shows the frequency response of tan-delta for these materials. Any fluctuations in this figure which have a width below an order of magnitude in frequency can be regarded as experimental noise. As a consequence of this, the loss of the unfilled materials between 1 and 1000 Hz has an uncertainty of two orders of magnitude. In the Nanoblend systems, two relaxation processes are evident. At 60 ℃ these are at around 10 Hz and 1 kHz respectively. These could be assigned to the α-relaxations of the LPE and BPE-rich phases respectively [5.12], in which case the filler would be simultaneously acting as a dielectric probe and modifying the underlying

molecular dynamics (as seen in the slight variation in peak frequencies between the two loading levels.) Nonetheless, without more in-depth experiments, one cannot rule out the possibility that relaxations are occurring more locally within the compatibilizer; neither can one forget that a wide range of MWS relaxation times could arise from subtle differences in the clay size distribution. The former case critically depends on the presence of unknown quantities such as heavy metal content and chemical byproducts from the compatibilisation process. As discussed in Chapter 2, it was not possible to obtain quantitative information pertaining to these factors.

Variable temperature experiments on NB20 could not be completed because the samples tended to present a low resistance path to the analyser which prevented measurements being taken. It is believed that this was due to charge carrier percolation through the particle networks. Nonetheless, room temperature experiments on three independent samples were able to be taken; these demonstrated a massive low frequency interfacial interaction which resulted in a tan-delta up to 100% higher than in NC20.

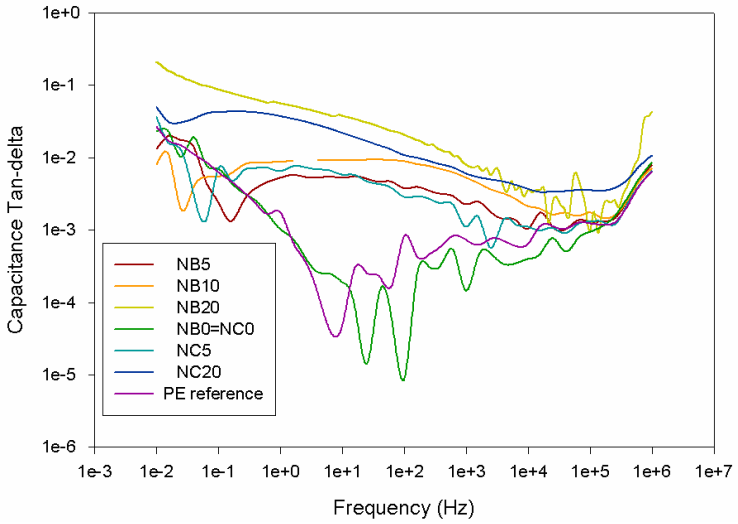

Figure 5.2: Room temperature loss data for various masterbatch compositions and loading levels.

This would suggest the existence of charge transport over much longer length scales in NB20. This is either because NB20 has a different particle size distribution to NC20 or it is a consequence of higher carrier mobilities in NB20.

The effect of interfacial polarisation on the real permittivity is shown in Figure 5.4, in which the data have been normalised to a universal average value at 1 MHz due to a lack of systematic variation. This value, at $\varepsilon_r = 2.19$ is low for polyethylene, which typically has $2.25 < \varepsilon_r < 2.3$ [5.1]. This is due to the fact that the cell did not have a guard electrode to ensure field uniformity. Rather, some of the flux will have been taken by the PTFE case, which has a lower ε_r of ~ 2.0. The interesting feature of Figure 5.3, however, lies in the fact that the normalisation process only removed an experimental range of 5%, with no apparent trend in ε_r with clay loading level. It was anticipated that the clay would significantly increase ε_r even at higher frequencies.

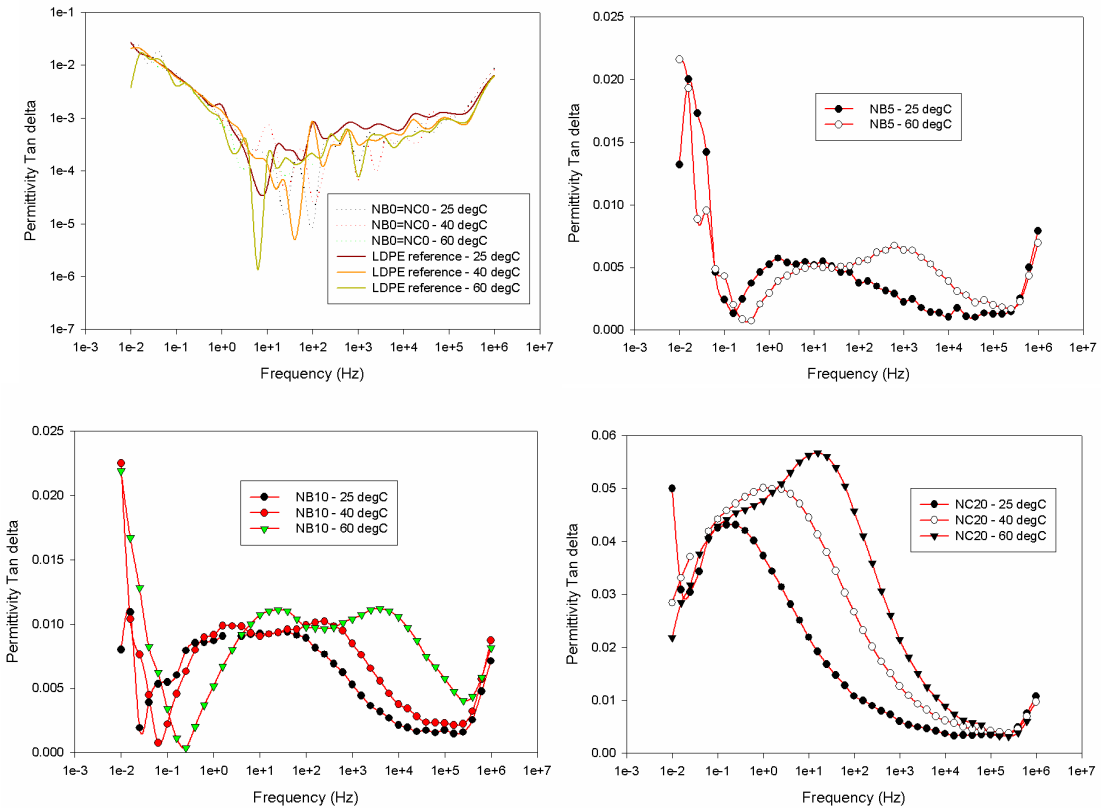

Figure 5.3: Loss characteristics as a function of frequency. No thermally activated behaviour is seen in the unfilled materials. NB5 and NB10 exhibit similar behaviour, contrasting that of NC20. NB20, not shown, is dominated by a massive low frequency interfacial interaction with tan-delta roughly halving every 2 decades from 1.2 at 10 mHz.

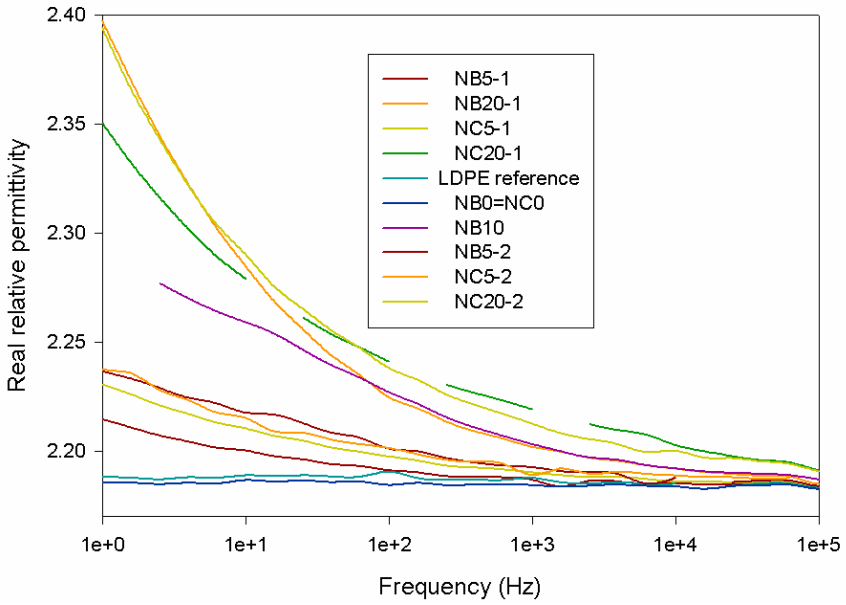

Figure 5.4: Real permittivity of the materials as a function of clay content. Increasing degrees of interfacial polarisation are seen as the clay content increases. The high frequency permittivity is remarkably unchanged.

5.3 Discussion of dielectric properties

The previous section implied that the high frequency relative permittivity in these materials is independent of composition. This is a surprising result which invites further analysis. A primitive estimation of the permittivity of a composite can be made as follows [5.13]:

$$\varepsilon_c = (1 - v_2)\varepsilon_1 + v_2\varepsilon_2 \qquad (5.4)$$

where ε_c, ε_1 and ε_2 are the relative permittivities of the composite and of the base and included phases respectively, q being the filler loading level as a fraction of the total volume. A better estimation can be made using the Maxwell-Wagner-Sillars high frequency result for ε_r[5.14]:

$$\varepsilon_\infty = \varepsilon_1 \frac{\varepsilon_1 + [A(1-v_2)+v_2](\varepsilon_2 - \varepsilon_1)}{\varepsilon_1 + A(1-v_2)(\varepsilon_2 - \varepsilon_1)} \quad (5.5)$$

Here, A is a shape factor for the filler phase which arises from the distortion of the local field by the filler particles. For spheroids aligned with their field along their long axis, $0 < A < 1/3$, whereas for spheroids aligned with their short axis parallel to the field, $1/3 < A < 1$. Perfect spheres correspond to $A = 1/3$. The equation assumes uniform orientation and particle distribution; more advanced treatments would require simulation [5.15].

Experiments using I30P sintered in the Graseby Specac press using a specialist die indicated an ε_r of >200 at 0.1 Hz, reducing to >10 at 1 MHz. Sintering was used both to reduce the amount of air in the sample and to produce a well-defined geometry. NC20 and NB20 contain 16.7 %wt masterbatch, which corresponds to ~7% wt o-MMT. The density of the I30P powder, determined by displacing hexane in a measuring cylinder, was evaluated as 1.7. Making the crude assumption that any density changes during intercalation are exactly offset by reductions in the volume-specific ε_r of the o-MMT (as per equation 5.4), we can consider an effective composite containing 4 vol% inclusions of $\varepsilon_r = 10$ material. Equation 5.4 then predicts a 14% increase in ε_r, which is too large to be masked by the ±5% experimental scatter.

However, as Figure 5.5 demonstrates, a MWS model with a shape factor of >0.6 could easily explain the observed lack of permittivity increase. In this scenario, the o-MMT would be present as oblate discoids orientated perpendicularly to the field. This morphology could be generated by a volume-exclusion effect through melt pressing, and is from that point of view consistent with the NB20 morphologies of Chapter 3. It was noticed during the WAXS experiments of Chapter 2 that by placing the extrudates with their axes perpendicular to the X-ray beam, the low angle scattering pattern developed considerable eccentricity in reciprocal space so as to indicate a large measure of clay orientation parallel to the axis. For this reason, it was decided when preparing disks for dielectric spectroscopy and electrical breakdown measurements to reduce the level of orientation by loading the extrudate pellets into the die with the extrudate axis in line with the pressing direction. It

is still possible, however, that a certain amount of over-compensation occurred and that the clay became partially aligned parallel to the sample surface. One must also bear in mind that it is the electrical rather than the strictly physical geometry which is important here: an individual clay particle may be physically spherical but have an ellipsoidal permittivity arising from anisotropic carrier mobilities due to the alignment of the silicate sheets within the particle. Alignment of this kind may take place via the flow field experienced by the compatibiliser molecules during pressing.

There are however several other mechanisms that could explain the lack of permittivity increase:

● The complex topologies present particularly in the Nanocor systems could give rise to multifarious screening effects.

● The molecular mobility of the polyethylene matrix may be reduced, either locally in the o-MMT – PE interaction zone or through more subtle changes in the hierarchically-constrained cluster interactions in the Dissado-Hill sense [5.7]. Anomalously low nanocomposite permittivities are common in the literature, and are commonly explained in terms of constrained molecular motion [5.16]. Priestly *et al.* [5.17] reported a lower-intensity *ß*-relaxation in PMMA / silica nanocomposites as a consequence of hydrogen bonding between PMMA ester side groups and hydroxyl units on the surface of the silica.

● The hydration state of the clay may be substantially altered by dispersion. It is known that the clay exhibits a series of relaxations from low frequency intra-gallery ionic motion to high frequency (>5 GHz) water dipole rotation. The response will be affected by the relative fractions of free and bound water [5.18].

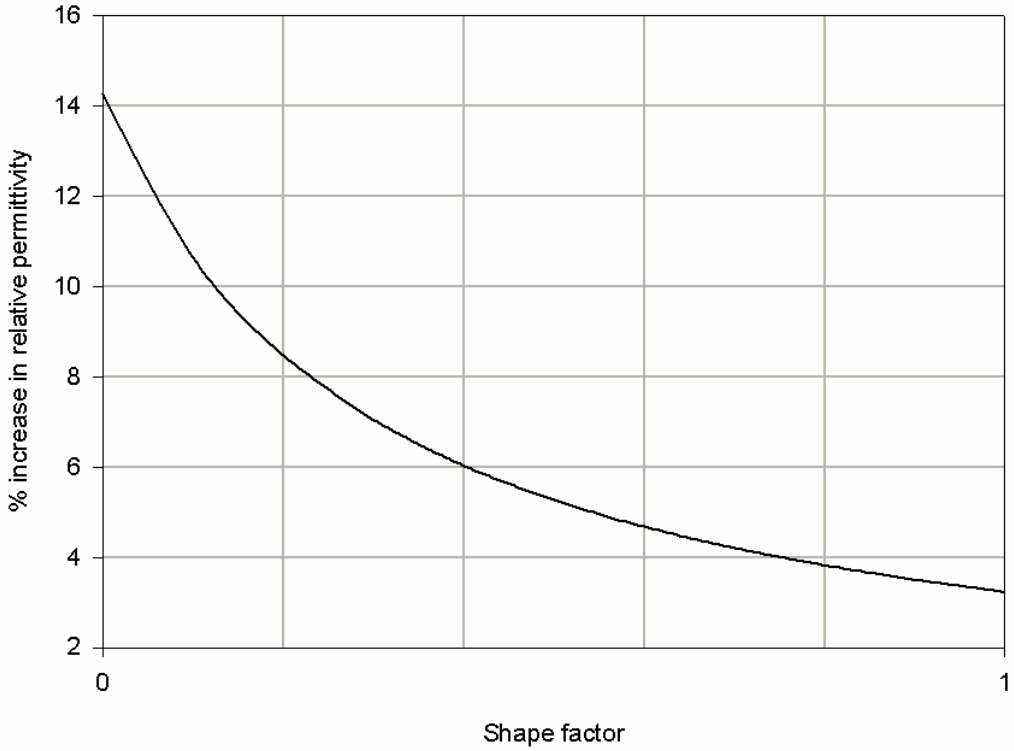

Figure 5.5: Effect of included phase shape parameter on percentage increase in composite permittivity. Based on ε_{clay} = 10 and $\varepsilon_{NB0=NC0}$ = 2.19.

Water is known to have a large effect on the low frequency dielectric response of nanocomposites. Roy *et al.* [5.19] and Zou *et al.* [5.20] have reported the presence of quasi-DC conductivity in silica / XLPE and silica / epoxy nanocomposites. This corresponds to a straight line on a Cole-Cole plot or, equivalently, parallel slopes for Re(ε) and Im(ε) on a Bode plot and is interpreted as percolation of charge carriers through overlapping water shells.

Zhang and Stevens [5.21] compared the dielectric responses of a polar matrix, epoxy, and a nonpolar matrix, LLDPE, upon filling with nanoalumina. When the epoxy contained 0.4% wt water, a distinct water relaxation was observed. The behaviour of this relaxation differed with nanofilling, implying that the nature of the water binding sites was altered. In particular, above -30 ℃, the relaxation showed anomalous behaviour by moving to lower frequencies with increasing temperature. This was interpreted as the water

changing from a bound to a freely dispersed state that did not exhibit thermal activation. Interestingly, no interfacial response was observed in the dried epoxy samples. In the LLDPE-based samples, it was found that a water content of only 0.06 %wt was sufficient to produce the same anomalous splitting in the low frequency peak. Clearly then, the low frequency dielectric response of nanodielectrics can be strongly humidity-dependent, and this could pose huge problems for the design engineer. In fact, MMT has been investigated for use in commercial humidity sensors [5.22].

It is possible that the large dielectric losses seen in all the loss peaks of Section 5.2 above are the result of impurity ions such as octadecylammonium chloride left over from the compatibilisation process. Montanari *et al.* [5.23] discovered a new relaxation in EVA–synthetic fluorohectorite nanocomposites which was attributed to a MWS relaxation. Washing the filler thoroughly in de-ionised water before compounding reduced the peak amplitude by a factor of four.

5.4 Dynamic Mechanical Thermal Analysis (DMTA)

A Rheometrics RSAII DMTA was used in dual cantilever mode. A sample measuring 4 mm * 40 mm * 1.7 mm is clamped at both ends and subjected to vertical simple harmonic motion whilst the resulting force at the centre of the sample is measured. The sample was manufactured by melt pressing followed by quenching. The formula used to calculate the elastic modulus indicates the large experimental sensitivity to errors in the sample length and thickness:

$$E' = \left(\frac{F_m}{d_m}\right)\left(\frac{L^3}{2bh^3}\right)\cos(\delta) \qquad (5.6)$$

where F_m and d_m are the measured force and actuator displacement. L is the effective distance between the centre and the clamp; b and h are sample width and thickness respectively. Errors in F_m and d_m are minimised by the use of air bearings. Nonetheless, any error in the ratio length : thickness will be cubed in the modulus.

It was necessary for the applied strain rms amplitude to be constant over the whole -100 °C – 20 °C temperature range. The variation in sample stiffness over this range is considerable; a compromise therefore needed to be reached to mediate between the risks of signal weakness and force saturation. A sample strain of 0.4 % was therefore used. During initial experiments, the temperature was changed in 10 °C steps from -100 °C to 20 °C. The sample was allowed to equilibrate for 1 min at each temperature before initiating a frequency scan. It is believed that the temperature-controlled air flow rate was sufficiently high for the samples to reach equilibrium within this time frame. Due to the high level of scatter expected, extra care was taken to ensure that the samples were randomised. Ultimately, it was found that there was insufficient liquid nitrogen to generate enough data below room temperature. The data presented below are only obtained at 35 °C and above.

The curves in Figures 5.6 and 5.7 are the average of three sets of data, including the responses of an 80:20 BPE : LPE blend. This was included in order to compare the response due to the clay with the response one would expect simply by increasing the LPE fraction. In order to generate the curves in Figure 5.7, the following relationships were used to obtain the compliance data:

$$J^* = \frac{1}{E^*} \tag{5.7}$$

$$J' = \frac{E'}{(E')^2 + (E'')^2} \tag{5.8}$$

$$J'' = \frac{E''}{(E')^2 + (E'')^2} \tag{5.9}$$

where *J'* and *J"* are the real and imaginary compliances; *E'* and *E"* are the real and imaginary moduli.

Consider first of all the real modulus and compliance data. No significant differences are seen between the filled materials and the 80 : 20 : 0 blend, any apparent differences being comparable to the experimental scatter. NB0=NC0 has a significantly smaller apparent modulus than the other materials, this difference being more apparent when interpreted in terms of a

larger compliance. Similarly, the imaginary modulus data do not vary significantly between the filled materials and the 80 : 20 : 0 blend.

Distinction between the filled and unfilled materials is seen both in the gradients of the real moduli with frequency and, more obviously, in the imaginary compliance data. The temperature / frequency range in question coincides with the crossover from viscoelastic to rubbery plateau behaviour. This is due to the oscillation period approaching the timescale of thermodynamic equilibration, leading to an entropic restoring force which manifests itself as an additional spring in a mechanical model. The imaginary compliance peak corresponds to coupling between slow moving entanglements [5.24]. The reduced peak intensity seen in the highly filled samples can be interpreted as pseudo-crosslinking at chain immobilisation

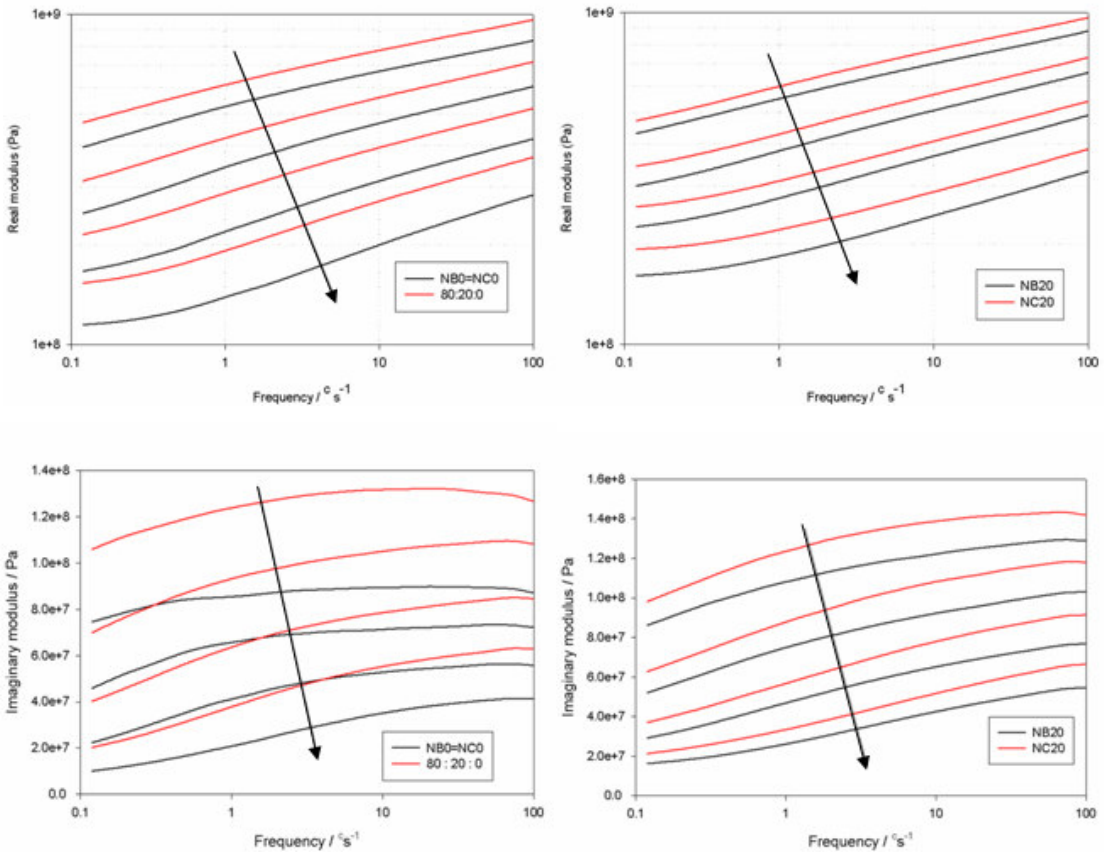

Figure 5.6: Real and imaginary modulus data for unfilled and highly filled materials. Arrow indicates direction of rising temperature: 35 °C, 45 °C, 55 °C, 65 °C. Each line is the average of 3 samples. No significant differences are seen between the filled samples and the 80 : 20 : 0 blend.

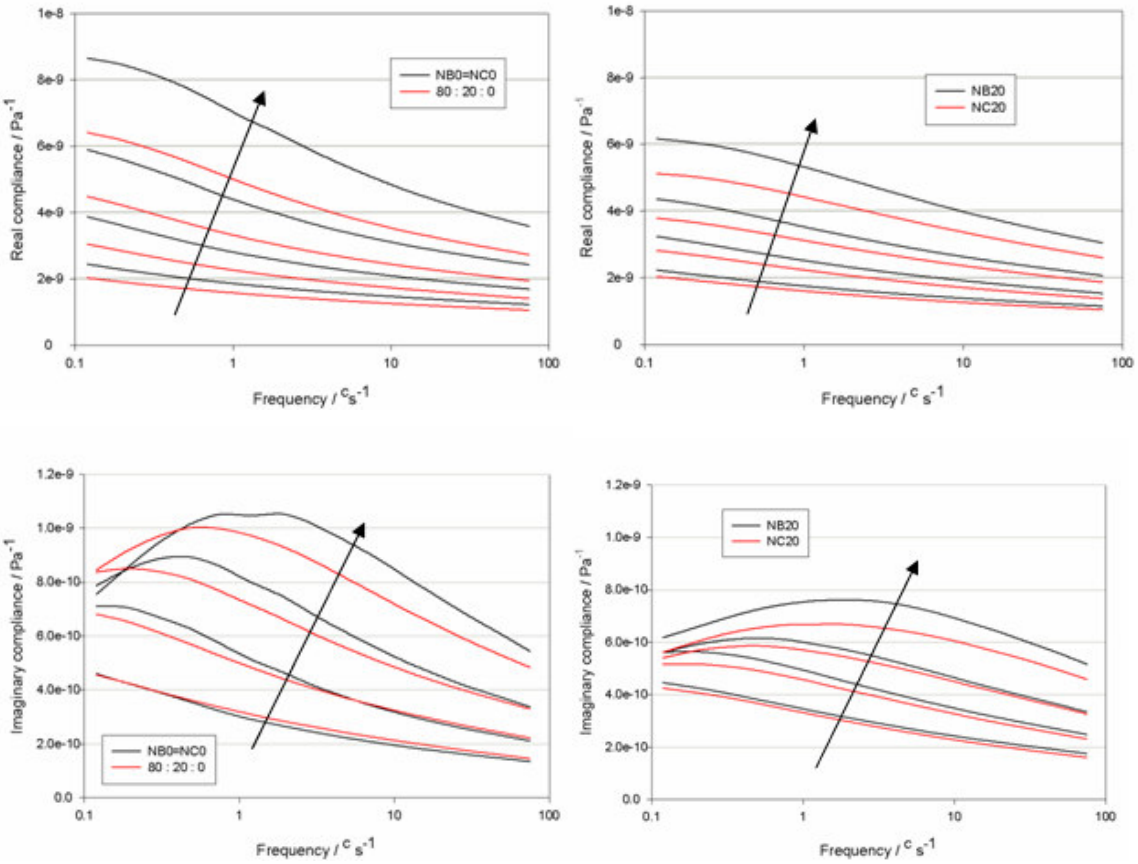

Figure 5.7: Real and imaginary compliance data for unfilled and highly filled materials. Arrow indicates direction of rising temperature: 35 °C, 45 °C, 55 °C, 65 °C. Each line is the average of three samples. The imaginary compliance response clearly distinguishes the filled and unfilled materials.

centers associated with the clay. These effectively screen the entanglements from the strain field.

It is sometimes possible to apply shift factors to curves obtained at various temperatures in order to obtain a frequency-temperature superposed master curve. The temperature dependence of these shift factors may then yield valuable information about the underlying physical processes. However, it is first necessary to identify those regions of the data for which the shift factors are independent of frequency, and to verify that the same shift factors apply for J' and J'' [5.24]. In this case, data at higher temperatures would be

required; this would involve the use of a melt rheometer and is therefore outside the scope of this work.

5.5 Large strain behaviour

Dynamic mechanical analysis, by its very nature, only yields information on the behaviour of the system below the limit of elastic behaviour; that is, before irreversible deformation takes place. Large strain behaviour involving strains of several hundred percent needs to be studied by tensile testing. Samples were prepared by melt pressing and quenching as before, and then cut into dumbbell shapes with the central loading portion measuring 25 mm * 4 mm * 1.7 mm. The samples were then clamped into the test grips of an Instron 4301 tensometer and pulled at 5 mm min^{-1} to a strain of 100 %. The results are shown in Figure 5.8. In these plots, a kink is seen at a stress of just below 7 MPa. This corresponds to a compliance liberated by overcoming the mass of the lower jaw, due to a loose coupling pin. Each of the traces can be split into two main regions before failure:

● Below 5% strain, the stress is approximately linear with strain. In this region, the energy supplied is mainly stored elastically, facilitated by a linearly increasing stress. Nonlinearity is mainly due to the decreasing cross-sectional area, though a small amount of compliance may be due to the sample bedding in to the grips.

● Above 5% strain, the yield stress is reached: the sample yields as sufficient energy is available to initiate a plastic deformation zone called a neck. As elements of this neck strain-harden, the extra incremental strain must be taken up by the remaining elements. Progressive elemental hardening occurs and the neck propagates along the sample [5.25]. This process is termed cold drawing.

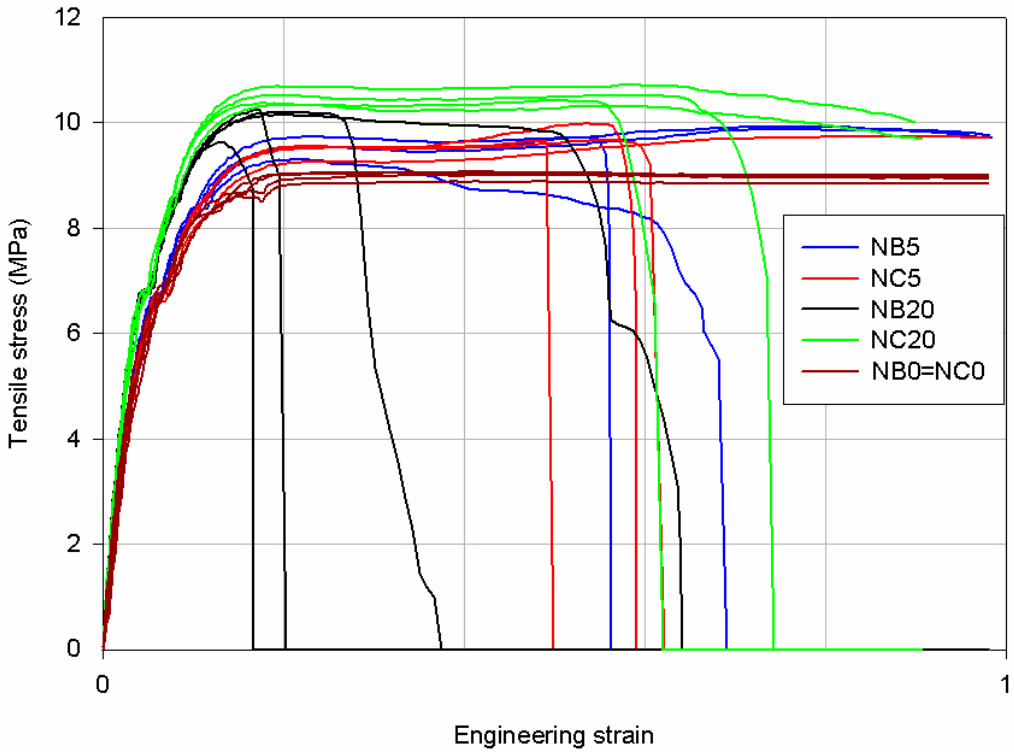

Figure 5.8: Tensile behaviour as a function of loading level and masterbatch composition. Three features can be seen: (1) The yield strength increases with loading level. (2) The filled samples (excepting NB20) undergo double yielding. (3) NB20 is particularly brittle.

Ultimate failure may be governed by processes from the macroscopic to the molecular. If the material does not undergo significant strain hardening, simple geometrical thinning may determine the failure stress. Alternately, a shear band may propagate diagonally across the sample. This can be understood in terms of Coulomb's hypothesis [5.26] whereby the shear yield strength along any chosen plane linearly increases with the stress normal to that plane. The shear band angle is then determined by the intrinsic coefficient of friction.

Alternatively, the material may undergo brittle fracture. Local elastic energy in a material may be relieved through the nucleation of a void. Under energetically favourable conditions, these may coalesce and form eccentric

cavities with their long axis normal to the stress field [5.27]. Such “crazes” contain many transverse fibrils which correspond to interlamellar tie chains which were constrained during the opening up of the amorphous region. These may then propagate as cracks through the material.

Failure may, in the case of semicrystalline polymers, be preceded by a morphological transformation whereby crystallites partially unravel and form fibrous structures. This may be accompanied by mechanical twinning of the crystals and is the formative mechanism of ultra-high modulus PE fibres [5.28].

The striking feature of Figure 5.8 is the low ultimate strength of NB20. This material was the only one to fail in a brittle mode. An SEM micrograph of the break surface can be seen in Figure 5.9 below.

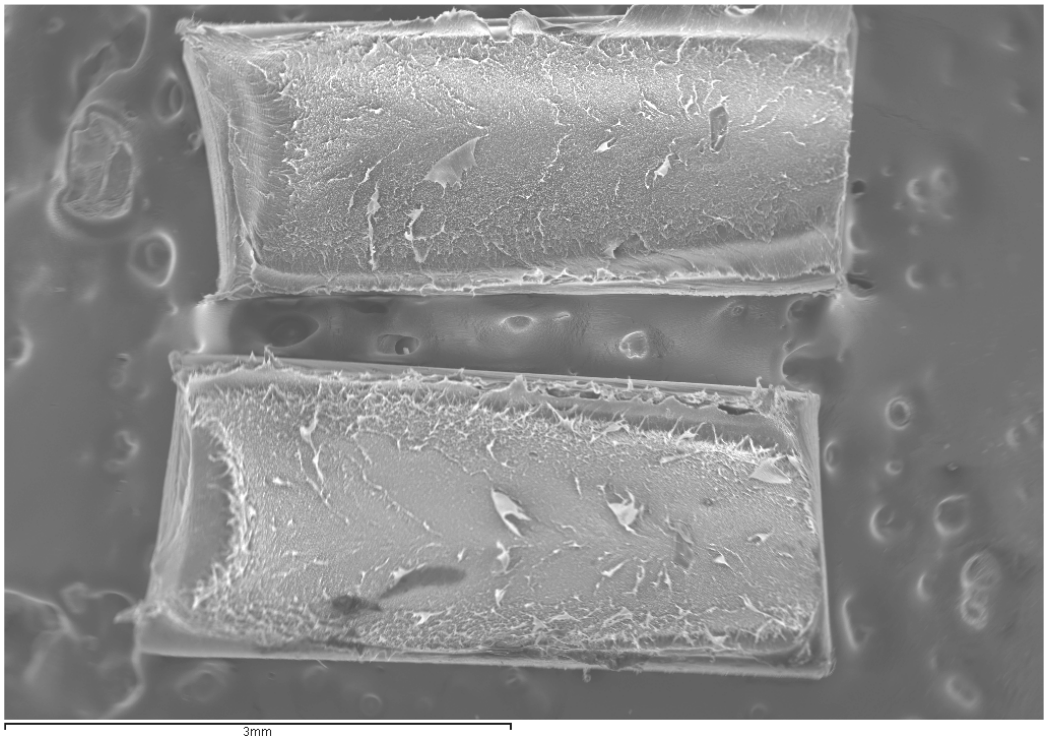

Figure 5.9: Two halves of a tensile fracture belonging to material NB20.

In Figure 5.8, the yield stress varies significantly only with the masterbatch loading level. This implies that the reinforcement effect of the clay is more strongly a function of loading level than of any differences that exist in the particle size distributions. Examining the initial gradient, NB20 and NC20 yield an elastic modulus increase of ~15 % above NB0=NC0, comparable to the DMTA data. However, in terms of absolute magnitude the latter are over 100%

larger than the results obtained with the tensometer. This is not serious; the cubic relationship of equation 5.6 requires only a 5% uncertainty in sample effective length : thickness for this to occur.

Despite the similarity in behaviour between NB20 and NC20 revealed in Figure 5.8, their failure mechanisms are remarkably different. Figure 5.10 is an SEM micrograph showing the post-failure highly fibrillated morphology of NC20.

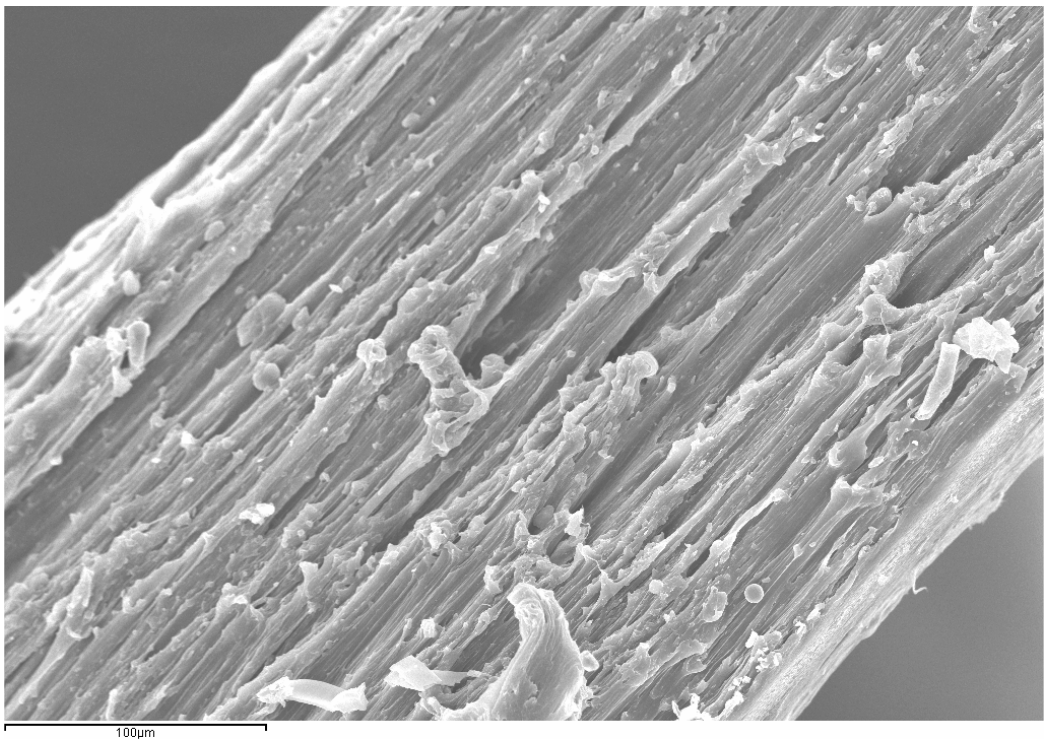

Figure 5.10: Post-failure fibrillar deformation observed in NC20. Strain direction from bottom left to top right of image.

Figure 5.11 is a lower magnification image of the same material at the tips of the failed regions. The trumpet-like openings are a standard feature of the post-failure NC20 morphologies. They can be seen in their incipient stage in Figure 5.12 and can also be observed in material NC5 (Figure 5.13.)

On the basis of Figure 5.12, the following model might be postulated for the formation of a trumpet. Firstly, an enhanced stress exists at the particle that can be seen sitting at the “mouthpiece” of the trumpet. If the matrix-agglomerate bonding is sufficiently weak, a void will open up and grow into a

tube. This will continue to grow as high levels of strain hardening take place in the walls. The question remains as to which end of the tube is fed with fresh material to grow. From Figure 5.12, it looks like that, at least in the early stages of growth, material is fed by the crazing zone on the other side of the particle. The crazes would facilitate compliance by converting deviatoric to hydrostatic stress. However, it is clear that this process cannot go on for ever. Taking the working hypothesis that the morphology of Figure 5.10 is a very advanced version of that shown in Figure 5.12, material must also be strain-hardened at the other end of the tube.

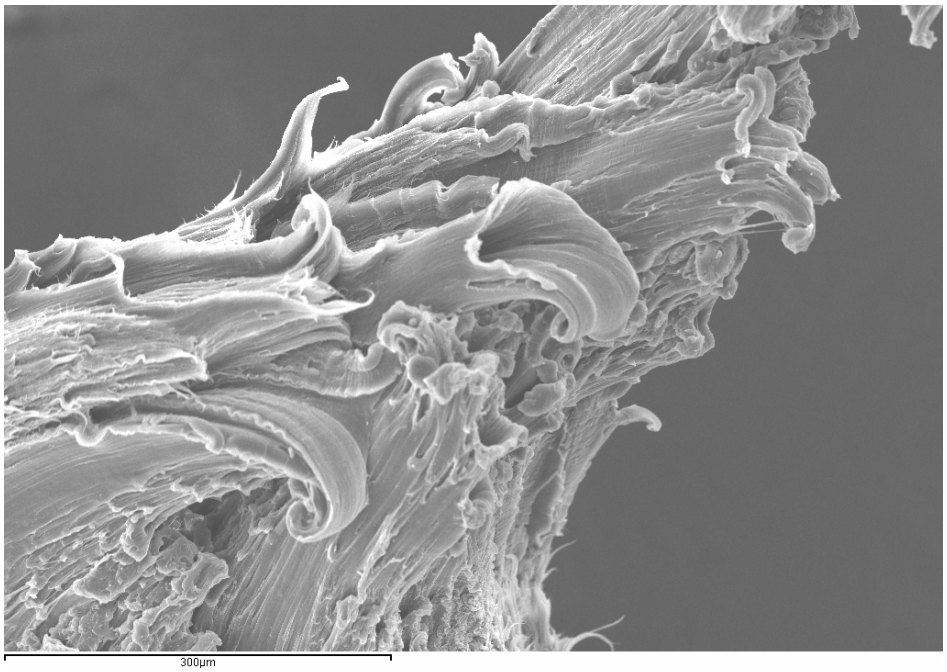

Figure 5.11: SEM micrograph showing tip of failure zone for NC20. The structure is dominated by trumpet-like features.

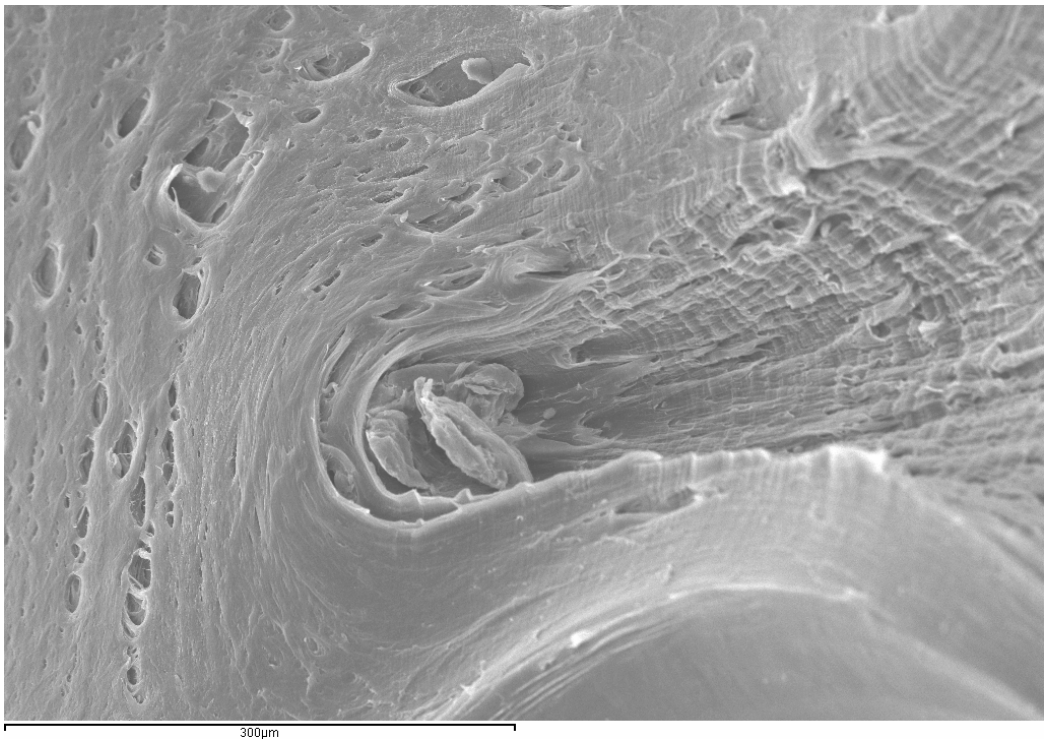

Figure 5.12: Post-failure image of NC5 showing a large agglomerate at the origination site of a trumpet-like feature. Crazes can be seen on the left hand side of the image.

A feasible mechanism for this is shown in Figure 5.13. A pellet of NC20 was placed on a glass slide and heated to 200 ℃ on a hot plate. It was squashed by pressing down onto the cover slip with a cork, followed by shaking in air to cool it. By analysing the material under crossed polars, its birefringence can be imaged. The large black objects correspond to air bubbles. (Since they contain no polymer, there is no opportunity for the plane of polarisation of light to be rotated and pass through the analyser.) The key feature of the air bubbles is their very high surface energy due to their non-spherical shape. Their tension appears to be taken by rope-like structures. Most likely, these consist of highly entangled polymer chains and clay aggregates. It is not difficult to see that these might form the machinery for tube pulling and subsequent strain-hardening of the tube walls. Is this then the dominant mechanism for tube pulling? Could it be that it is in fact the only mechanism: that far from nucleating the tube, the clay agglomerate actually terminates it by blunting?

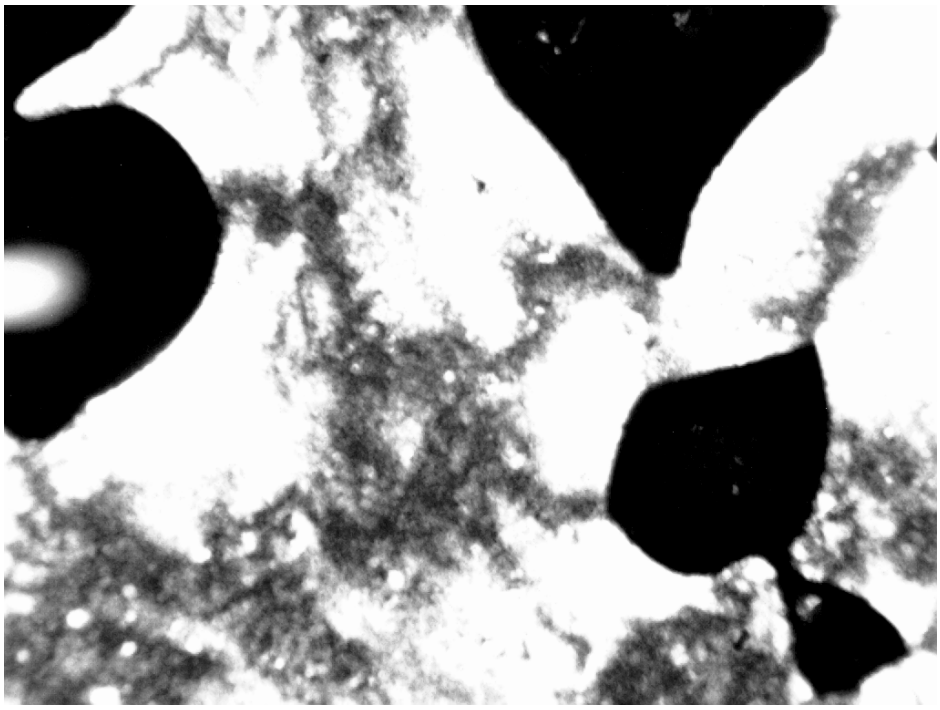

Figure 5.13: Polarised optical micrograph (POM) of material NC20, following squashing at 200 °C. Image width 100 µm. High levels of energy are associated with the air bubbles (large black objects.)

The crazing would rather feed material not into the tube walls but into the surrounding region. Of course, it is not impossible that the crazed region itself corresponds to the blunting process and that the agglomerate has simply fallen to the bottom of the tube due to the shock of failure.

Whatever the mechanism for the reinforced tube formation, it serves to toughen the material. The converse situation is seen in material NB5, shown in Figure 5.14 below. With no obvious toughening mechanism, local stresses have become intensified between clay particles where polymer is constrained. Increased hydrostatic pressures have led to voiding and microscopic necking. It is easy to see that increasing the loading level by factor of four (as per NB20) could lead to stress fields that would be energetically favourable for crack propagation.

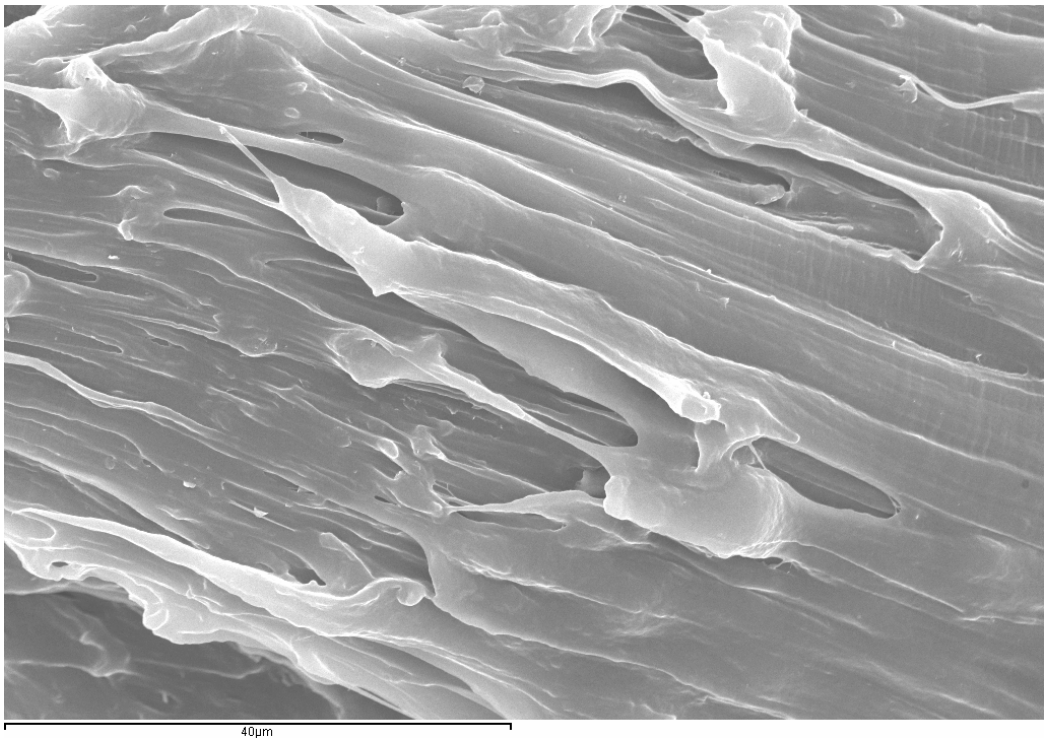

Figure 5.14: Post-failure image of material NB5. Clay particles have constrained the polymer, resulting in local stress enhancement and ductile failure.

Finally, consider Figure 5.15, which compares the effect of hot-plate squashing on the materials for differing loading levels of each masterbatch. Regardless of the bubble properties, the background image of NC5 is more birefringent than even NB20, showing a greater amount of anisotropy. On the other hand, materials NB20 and NB0=NC0 are indistinguishable in this experiment. Nonetheless, even material NB5 exhibits double necking behaviour in Figure 5.8. Yielding in NB0=NC0 leads to indefinite cold drawing, whereas both NC5, NB5 and NC20 strain harden at an engineering strain of 0.7 before developing another neck. It seems therefore that in the Nanocor systems, at least two strain hardening processes are operating: at the local level as a toughening mechanism and at a macroscopic level to drive multiple necking. Whereas the second process is relatively insensitive to particle size distribution, the former is not.

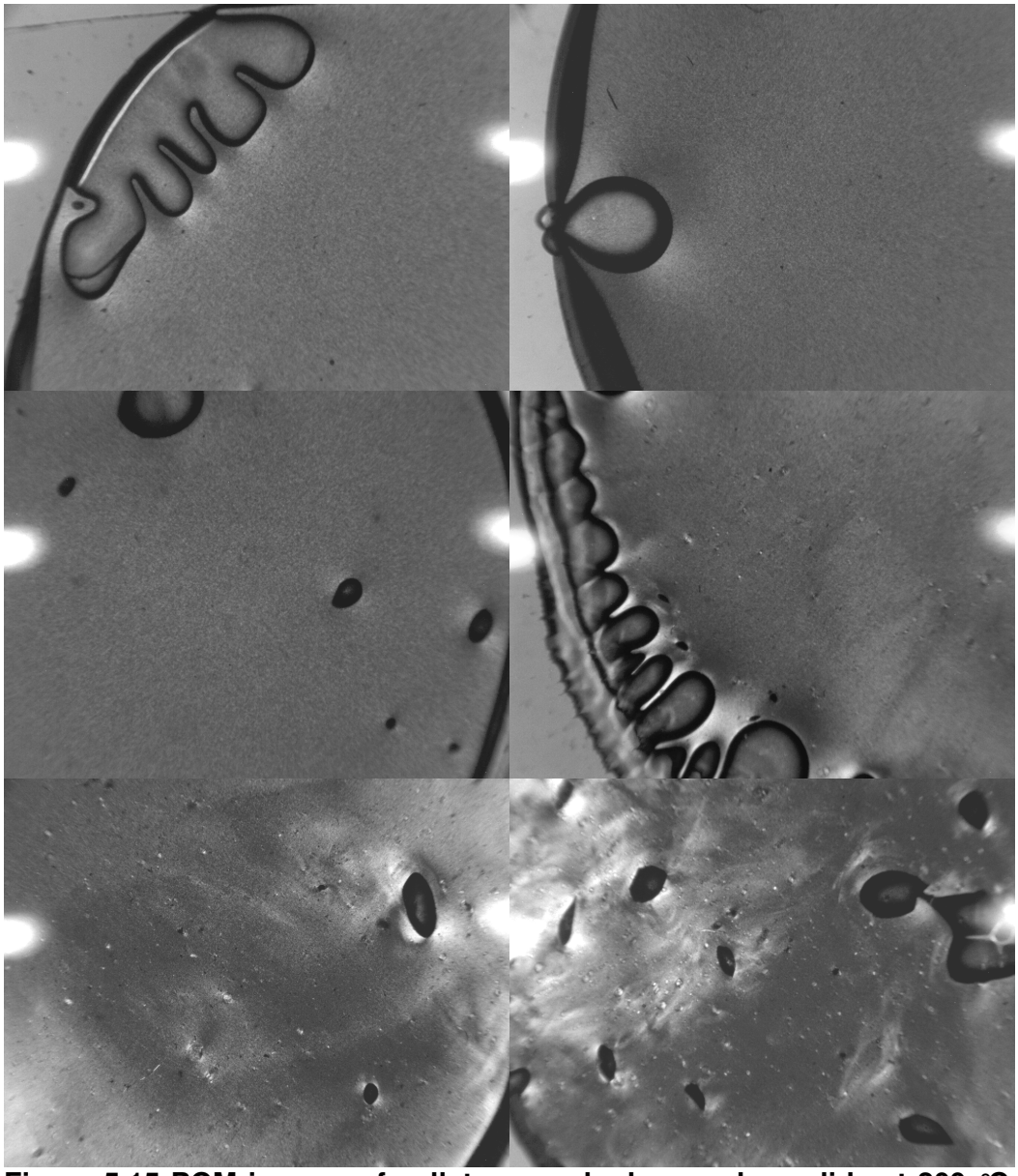

Figure 5.15 POM images of pellets squashed on a glass slide at 200 ℃. Upper left: NB0=NC0. Upper right: NB5. Middle left: NB20. Middle right: NC5. Bottom left: NC10. Bottom right: NC20. Image widths 500 µm. More birefringence is seen at the lowest Nanocor than the highest Nanoblend loading level.

5.6 Discussion of mechanical properties

As opposed to their controversial and poorly understood electrical properties, nanocomposites are comparatively well understood from a mechanical point of view. The current interest in layered silicate polymer nanocomposites can be traced to the early 1990s, when researchers at Toyota prepared nylon-6/clay nanocomposites by in-situ polymerization. They reported that these materials exhibit a 50% increase in strength and a doubling in elastic modulus over the base resin, together with an increase of 80 ℃ in heat distortion temperature [5.29]. A decade on, polymer/layered-silicate (PLS) nanocomposites can now be found in diverse automotive applications by virtue of their improved mechanical properties, ranging from timing-belt covers and fuel-system components to doors and seats [5.29]. The comprehensive article by Tjong [5.30], summarized briefly here, reviews the enormous amount of research into the mechanical behaviour of nanocomposites that has been undertaken in the last decade. In general, silicate platelets have a strengthening and stiffening effect on the base polymer, but they tend adversely to affect the toughness and tensile ductility of semicrystalline polymers. Such behaviour is consistent with that of material NB20. Glassy polymers can also suffer from brittleness resulting from the difficulty of dispersing the clay in such systems. On the other hand, the toughness of elastomers and epoxy resins is generally improved, due to microcrack deflection. Greater toughness can also be obtained with nanoceramic particles, due to cavity formation and shear yielding effects.

In an attempt to understand these phenomena, micromechanical models have been extrapolated to the nanometric level, even taking into account effects such as incomplete exfoliation in clay/polymer nanocomposites [5.31]. Silicates and carbon nanotubes have aspect ratios of ~200 and ~1000 respectively, and so their intrinsic capability for matrix reinforcement is enormous. It must not be forgotten, however, that the filler-matrix interaction zone is capable of behaving in a completely different manner to that of the bulk polymer. For example, Shah *et al.* [5.32] observed that the addition of an organically modified clay to poly(vinylidene fluoride) (PVF_2) resulted in a change in the dominant crystal form from the usual α to β and the

production of material with enhanced stiffness and toughness. Alternatively, changes in the glass transition temperature would serve to alter the mechanical properties of glassy systems. Although in our case the highly filled materials were compared to an 80 : 20 w/w HDPE : LDPE blend, there is in fact no evidence from Chapters 3 and 4 of higher crystallinity in the filled systems. However, this does not rule out the possibility that their mechanical properties might be determined by the topology not only of the distributed clay but also of the crystalline phase.

The deformation morphology of NC20 is particular interesting because of the implication that long range interactions are present in the material. The implication is that the material may have a long memory of local strain history, potentially explaining the differences in isothermal crystallisation morphology between NC20 and NB20 discussed in the previous chapter. Rheological studies performed on melts have shown that mesoscopic percolative networks of clay lead to pseudo-solid behaviour whereby the dynamic modulus becomes progressively independent of oscillatory shear frequency [5.33]. Furthermore, some researchers have found that melt rheology is a potentially useful tool for determining the degree of exfoliation [5.34]. If this is the case, then we have substantial evidence that the Nanocor systems contain a larger amount of fully exfoliated material than the Nanoblend systems. Since it also contains much larger agglomerates, it then follows that the particle size distribution is narrower in the Nanoblend material.

5.7 Conclusions

Dielectric spectroscopy has shown that both masterbatches lead to large increases in the dielectric loss. At low frequencies, this is most likely due to the conduction of Cl^- ions between interfaces, which could be eliminated by adopting a thorough cleaning procedure after the organocompatibilisation process. However, if the matrix itself is rendered dielectrically active by the masterbatch chemistry, then these materials would still be completely unsuitable for AC cables. Mechanically, small yet significant increases are seen in the elastic modulus, driving up their necessary bend radius on a cable drum and therefore installation cost. Furthermore, although the Nanocor

systems are intrinsically tougher than the Nanoblend ones, the potential presence of very high local strains and long shear history memories may cause problems for a commercial production process. NC20 could perhaps provide novel opportunities for exploitation in other areas such as the inexpensive production of microtubes for microfluidic devices, but the conclusion of this chapter must be that as far as electrical insulation systems are concerned, these materials present considerable challenges for further development.